

# Bright Debris Disk Candidates Detected with AKARI/Far-Infrared Surveyor (FIS)

Qiong Liu<sup>1</sup>, Tinggui Wang<sup>1</sup>, Peng Jiang<sup>1</sup>

## ABSTRACT

We cross-correlate *Hipparcos* main-sequence star catalog with *AKARI/FIS* catalog, and identify 136 stars (at  $> 90\%$  reliability) with far-infrared detections at least in one band. After rejecting 57 stars classified as young stellar objects, Be stars and other type stars with known dust disks or with potential contaminations, and 4 stars without infrared excess emission, we obtain a sample of 75 candidate stars with debris disks. Stars in our sample cover spectral types from B to K with most being early types. This represents a unique sample of luminous debris disks that derived uniformly from an all sky survey with a spatial resolution a factor of two better than the previous such survey by *IRAS*. Moreover, by collecting the infrared photometric data from other public archives, almost three quarters of them have infrared excesses in more than one band, allowing the estimate of the dust temperatures. We fit the blackbody model to the broad band spectral energy distribution of these stars to derive the statistical distribution of the disk parameters. Four stars with excesses in four or more bands require a double blackbody model, three of them are clustered around (100, 40)K and the other ( $\sim 200$ , 50)K.

*Subject headings:* main-sequence stars — infrared excess: stars — circumstellar dust

## 1. Introduction

Our solar system is a debris system with the asteroid belt at 2 - 3.5 AU and the Kuiper belt at 30 - 48 AU (Kim et al. 2005). Debris disks have been detected in extra-solar stellar systems as well, commonly referred to as “The Vega Phenomenon” (Silverstone 2000). The stars with debris disks are generally much older than 10 Myr (Krivov 2010),

---

<sup>1</sup>Key Laboratory for Research in Galaxies and Cosmology, University of Science and Technology of China, Chinese Academy of Sciences, Hefei, Anhui 230026, China; jonecy@mail.ustc.edu.cn; twang@ustc.edu.cn

which is much longer than the typical time scale of collisional destruction of dust grains or of spiraling inward due to Poynting-Robertson drag. Thus dust grains have to be continuously replenished by collisions and/or evaporation of planetesimals (Backman & Paresce 1993; Wyatt 2008). The studies of debris systems are significant because they provide a better understanding of the formation and evolution of planetesimal belts and planetary systems (Zuckerman & Song 2004; Moór et al. 2011; Raymond et al. 2011, 2012).

The first extra-solar debris disk was detected by the *Infrared Astronomical Satellite* (*IRAS*) around Vega in 1983 (Auman et al. 1984). Up to now, nearly a thousand debris disks have been detected. Most of these systems were found through the detection of infrared (IR) excess over the stellar photospheric emission. The IR excess is explained as the dust re-radiation of the absorbed starlight. At the sensitivity level of the Multi-band Imaging Photometer (MIPS) on *Spitzer* (Werner et al. 2004; Rieke et al. 2004), the incidence of debris disks around main-sequence (MS) stars is about 15% (Krivov 2010). Due to their small sizes, only dozens of debris disks around nearby stars have follow-up direct imaging observations in optical, mid-infrared (MIR), and sub-millimeter bands (e.g., Schneider et al. 2001; Greaves et al. 2005; Wyatt et al. 2005; Kalas et al. 2006; Su et al. 2008; Lagrange et al. 2012; also see <sup>1</sup>).

The observed debris disks display diverse properties. Most debris disks have relatively low dust temperatures between 30-120 K, corresponding to disk sizes from several tens to a hundred AU for type A to K stars (Chen et al. 2006; Moór et al. 2011; Plavchan et al. 2009; Rhee et al. 2007). A small subset of warm debris disks have been discovered recently with *AKARI*, *Spitzer* and *Wide-field Infrared Survey Explorer* (*WISE*) (Fujiwara & Onaka et al. 2010; Meyer et al. 2008; Fujiwara & Ishihara et al. 2010, 2013; Olofsson et al. 2012; Ribas et al. 2012), and the incidence of such disks drops very rapidly with the age of the stars (Urban et al. 2012). More recently, *Herschel* revealed a population of cold debris disks extending to more than one hundred AU with its good sensitivity to the long IR wavelength (Eiroa et al. 2011). A single blackbody model usually provides a good fit to the MIR spectrum, suggesting that grains are distributed over a relatively narrow annulus (Schutz et al. 2005; Chen et al. 2006). The relatively narrow width has been confirmed for some debris disks by direct imaging in the IR and sub-mm bands (Booth et al. 2013).

The incidence of debris disks as a function of other stellar parameters is of great interest as it gives further clue to its origin. It appears that the frequency of stars with debris disks is larger among earlier type of stars, and decreases with the increases of stellar age (Rhee et al. 2007; Wyatt 2008). The rate appears to correlate with the presence of planets,

---

<sup>1</sup><http://www.circumstellardisks.org>

but not the metallicity of the host stars (Maldonado et al. 2012). The general trend with stellar age reflects the consumption of planetesimals during the system evolution. However, interpretation of the correlation with stellar types may be more complex since early type stars have much shorter life-time than late type stars and the correlation may be entirely caused by the age-dependence of incidence. In addition, the detected debris disks displayed a wide range of IR excesses from  $10^{-6}$  up to  $10^{-2}$  of stellar bolometric luminosity. Over such a wide range, different mechanisms of debris disk may operate, thus it would be interesting to examine the incidence at a certain fraction of IR excesses. To explore a large parameter space, a large unbiased sample of debris disks with known host parameters is required.

Up to now, debris disks have been discovered mostly based on the IR data from four satellites: *IRAS* (Mannings & Barlow 1998; Rhee et al. 2007), *Infrared Space Observatory (ISO)* (Kessler et al. 1996; Oudmaijer et al. 1992; Abraham et al. 1999; Habing et al. 1999; Fajardo et al. 1999; Spangler et al. 2001; Decin et al. 2003), *Spitzer* (Beichman et al. 2006; Bryden et al. 2006; Chen et al. 2005; Kim et al. 2005; Moór et al. 2006, 2011; Rebull et al. 2008; Rieke et al. 2005; Siegler et al. 2007; Su et al. 2006; Wu et al. 2012) and *Herschel* (Matthews et al. 2010; Eiroa et al. 2013). *IRAS* contained a cryogenically cooled telescope orbiting above the Earth’s atmosphere to make an unbiased all-sky survey at 12, 25, 60, and 100  $\mu\text{m}$  (Neugebauer et al. 1984) at a relatively poor spatial resolution ( $4' - 5'$ ) and sensitivity (0.6 Jy at 60  $\mu\text{m}$  in Point Source Catalog, 0.225 Jy at 60 $\mu\text{m}$  in Faint Source Catalog)<sup>2</sup>. *Spitzer* and *ISO* possess much better spatial resolutions and sensitivities than *IRAS* but cover much smaller area of sky at mid and far-infrared (FIR) bands. Thus the latter missions discovered more faint debris disks. The latter satellites also carried pointed observations of nearby bright stars that were sensitive to the IR excess down to  $10^{-6}$  of host star luminosity.

In this paper, we search systematically for debris systems around MS stars by cross correlation of the *Hipparcos* catalog (Perryman et al. 1997) with AKARI/Far-Infrared Surveyor (Kawada et al. 2007) All-Sky Survey Bright Source Catalogue (AKARIBSC, Yamamura et al. 2010). *AKARI/FIS* surveyed all sky at FIR with a spatial resolution (48 ") better than *IRAS* and at a sensitivity (0.55 Jy in 90  $\mu\text{m}$ ) comparable to *IRAS*. The higher resolution will significantly reduce the false contamination in comparison with *IRAS*. The same with the *IRAS* studies, our work also focuses on the IR bright debris disks that complement the deep surveys from *ISO* and *Spitzer*. Our primary motivation is to search for FIR excess stars by *AKARI/FIS* and discuss the fundamental parameters of the disks such as dust temperature, fractional luminosity and dust location. These parameters can be estimated

---

<sup>2</sup>See IRAS Explanatory Supplement, Assendorp et al. 1995, Allam et al. 1996

from the spectral energy distribution (SED) of dust emission. Fortunately, all IR excess stars except HIP 57757 in our sample have *WISE* detections which lead to better wavelength coverage than many previous searches. As shown by Moor et al. (2011), the interpretation of a SED is ambiguous, but by handling a debris disk sample as an ensemble, one can obtain a meaningful picture about the basic characteristics of the parent planetesimal belt(s) and about the evolutionary trends. The paper is arranged as follows. We will describe the data sets and methods used in the construction of the debris disk sample in Sect. 2; and present an analysis of the properties of the disks as well as their host stars in Sect. 3; In Sect. 4, we discuss the sample comparison; Finally, we present the conclusion in Sect. 5.

## 2. The Method and the Sample

### 2.1. Matches between *Hipparcos* catalog and AKARIBSC

The primary star catalog used in this work is the *Hipparcos* catalog, which contains over 110,000 stars with precise photometry as well as astrometry of unprecedented accuracy for the nearby stars (Bessell 2000). In Figure 1, we show a Hertzsprung-Russell (H-R) diagram for all the cataloged stars by extracting the colors ( $B-V$ ) and parallaxes from *Hipparcos* database. The MS stars are selected according to the criterion  $M_V \geq 6.0(B-V) - 2.0$  (Rhee et al. 2007). This results in a catalog of 67,186 *Hipparcos* MS stars.

We then cross-correlate the catalog with the AKARIBSC to identify the *Hipparcos* MS stars detected in the *AKARI/FIS* bands. Since the AKARIBSC has much worse position precision than the *Hipparcos* catalog, we determine the matching radius based on the performance of *AKARI* only. The spatial distribution of *AKARI/FIS* sources is very inhomogeneous on the sky, so a uniform matching radius is not an ideal choice. To show this, we write the false detection rate for a sub-sample of stars on the sky with the background surface density  $n$  of IR sources as follows,

$$R_{false} = \frac{N_{false}}{N_{total}} = \frac{N_* \pi r^2 n}{N_* f c(r) + N_* \pi r^2 n} = \frac{\pi r^2 n}{f c(r) + \pi r^2 n} \quad (1)$$

where  $f$  is the fraction of *Hipparcos* stars with IR fluxes above the detection limit,  $N_{total}$  and  $N_{false}$  are the number of all matches and the expected number of chance matches.  $c(r)$  is the completeness with a matching radius  $r$ , i.e., the probability of a real matching source falling within a circle of radius  $r$  around the star, which is determined by the position error ellipse of the IR source. Assuming  $n$  does not correlate with  $f$ , the fraction of false matching increases with the background surface density of IR sources at a given matching radius. In reality,  $f$  and  $n$  might be correlated, e.g., young stars are more likely located on the Galactic

plane, where stellar surface density is also higher; as such the false matching fraction may not follow Eq. 1 exactly. Anyway, we will determine the matching radius according to the surface density of IR sources. Since  $c(r)$  increases slower than  $r^2$ , as  $r$  increases, the false matching rate increases.

As a trade-off between the reliability and completeness, the matching radius at a given surface density is so chosen that false detection rate is less than 10 %. In practice, we estimate the local *AKARI/FIS* source density around each *Hipparcos* star, and then divide *Hipparcos* stars into different density bins. For each bin, we increase the matching radius iteratively from 5 ″, to a radius where the false detection rate is close to 10% or to the upper limit of 20 ″. The cross-correlation results in 136 matching pairs. Figure 2 presents the number of *Hipparcos* stars (upper panel), matched IR sources (middle panel), and matching radius (bottom panel) at each bin of the local IR source density. An interesting feature in this plot is that the peak of matched pair distribution is shifted to the high density area rather than to lower density area as expected. This implies a strong correlation between  $f$  and  $n$ . Regions of lower density have a lower fraction of stars with bright debris disks perhaps because the chance of finding young stars in such regions is lower. While at higher density regions, the higher excess fraction in the Galactic plane may be justifiable and the magnitude of this effect can be estimated from Figure 2 which looks like the fraction is fairly constant above  $\sim 1 \text{ deg}^{-2}$ , but a factor of 6 lower for lower far-IR densities.

Next, we remove the sources with obvious contaminations in the IR. Seven stars in nebula are rejected because nebula is a FIR source. Among them, three stars are in Kalas’s sample (Kalas et al. 2002); nebula is clearly seen in the images of other three stars returned by SIMBAD; and one additional star (HIP 78594) was rejected by Moór et al. (2006) based on the image of the Digitized Sky Survey, which shown a reflection nebulosity around this star. Another contamination source is the emission from cold diffuse interstellar dust (cirrus, Rhee et al. 2007), which also emit MIR (e.g., Boulanger et al. 1998). We reject the cirrus contamination stars based on their MIR images obtained by *WISE* (Wright et al. 2010). *WISE* has mapped the whole sky in four IR bands  $W1$ ,  $W2$ ,  $W3$  and  $W4$  centered at 3.4, 4.6, 12 & 22  $\mu\text{m}$  with 5  $\sigma$  point source sensitivities better than 0.08, 0.11, 1 and 6 mJy, respectively. The angular resolutions are 6′1, 6′4, 6′5 & 12′0 at corresponding bands, and the astrometry precision for high SNR sources is better than 0′15 (Wright et al. 2010). The high sensitivity and high angular resolution images are used to remove the confusion source and to further constrain the disk properties in the SED fitting. All stars except HIP 57757 are covered by *WISE*. We check the *WISE* images of these sources for the presence of weak diffuse emissions around stars. Seven stars are affected by potential cirrus emissions and rejected, leaving 122 stars for further study. Note that the number of rejected contaminated sources is in agreement with the expected chance matches.

## 2.2. Infrared Emission of Stellar Photosphere

Obtaining the flux densities of stellar photosphere is essential for identifying and measuring the strength of an IR excess (Bryden et al. 2006). We collect the optical to near-infrared (NIR) absolute photometric data of stars in our sample to construct SED. Optical magnitudes in  $B$  and  $V$  are taken from the *Hipparcos* satellite measurements. NIR photometries  $JHK_s$  are extracted from Two Micron All Sky Survey (2MASS) catalogs (Skrutskie et al. 2006). The observed magnitudes are converted into flux density (Janskys) using the zero magnitudes in Cox (2000) (Rhee et al. 2007).

The stellar SEDs are fitted with the latest Kurucz’ models (ATLAS9)<sup>3</sup> (Castelli et al. 2004). The models cover wide ranges of four parameters: temperature, surface gravity, metallicity, and projected rotational velocity. For each stellar type, we select only a subset of model spectra from ATLAS9 according to Allen’s astrophysical quantities (Cox et al. 2000). For B-type stars, the effective temperatures are in 500 K increments from 10000 to 20,000 K, the surface gravity  $\log g \text{ cm s}^{-2}$  value is 4.0. For A-type and later types stars, the effective temperatures are in 250 K increments from 3,500 to 10,000 K, the surface gravity  $\log g \text{ cm s}^{-2}$  values are 4.0, 4.5. We chose microturbulent velocity  $\xi=2 \text{ km s}^{-1}$  and metallicity value  $[M/H] = 0$  (solar metallicity) for all cases.

We fit the model spectra to the observed SEDs from optical to NIR for each object in order to find the best matched stellar models. During the fit, the stellar spectra are reddened and convolved with the response of each filter to yield the model flux density at each band. This method gives the model flux density more accurately than adopting a constant magnitude to flux conversion factor, especially when the passband includes significant spectral features such as the Balmer jump (Rhee et al. 2007). For each stellar model, the best fit is obtained by minimizing  $\chi^2$  with the extinction  $E(B - V)$  and normalization as free parameters. We select out the best model with the smallest  $\chi^2$  among different stellar models. Using the best-fit Kurucz model, we estimate the stellar photospheric flux densities in the *WISE* and *AKARI* bands.

To assess the reliability of stellar photospheric flux predicted by the best model in the *WISE*  $W3$  and  $W4$  bands, we examine the distribution of the differences between observed and predicted magnitudes for a sample of randomly selected *Hipparcos*MS stars, which usually should not show MIR excesses. The sample is so compiled that the comparison sample well matches our final debris disk sample in the distribution of Galactic latitudes, stellar spectral types as well as their optical magnitudes. The size of the comparison sample is a

---

<sup>3</sup><http://wwwuser.oat.ts.astro.it/castelli/grids.html>

factor of two larger. We fit the optical to NIR photometric data of the comparison sample with stellar models as described above. The distributions of the differences are fairly narrow with almost no systematical offsets (Figure 3):  $\langle W3(\text{observed}) - W3(\text{model}) \rangle \simeq 0.002\text{mag}$ ,  $\langle W4(\text{observed}) - W4(\text{model}) \rangle \simeq 0.04\text{ mag}$ , and  $\sigma(W3) = 0.06\text{ mag}$  and  $\sigma(W4) = 0.13\text{ mag}$ . In the following analysis, we will incorporate these numbers as the systematical uncertainties of model fluxes in the two *WISE* bands.

### 2.3. Identification of Debris Disk Candidates

Our goal is searching for the IR excess from debris disks, while debris disk is not the only source of the IR excess. So we will remove other IR excess sources from our sample. Firstly, in some young O stars, significant IR excess may arise from gas free-free emission instead of from the debris disk. These stars generate strong ionized winds that produce strong IR and radio excesses. Thus five O stars are excluded from our sample. Secondly, a Be star is a B-type star with prominent hydrogen emission lines in its spectrum and IR excess (Porter et al. 2003). Both emission lines and excessive IR emission in Be stars are formed in the circumstellar disks, that are most likely ejected or stripped from the stars themselves. We rejected 12 Be stars based on SIMBAD classification. Thirdly, we reject 3 objects including a star without reliable flux density of *AKARI/FIS* (none of the band has the quality flag=3), a quasar and a Post-AGB stars.

Finally, young stellar objects (YSOs) often harbor protoplanetary disks (Moór et al. 2006), and also display IR excesses. We will reject them according to the shape of their SEDs in the IR as follows. YSOs are classified observationally according to the shape of their SEDs in the IR between the K band (at  $2.2\ \mu\text{m}$ ) and the N band (at  $10\ \mu\text{m}$ ) defined as (Armitage 2007),

$$\alpha_{\text{IR}} = \frac{\Delta \log(\lambda F_{\lambda})}{\Delta \log \lambda}, \quad (2)$$

where  $\alpha_{\text{IR}} > -1.5$  is a strong indication for a YSO. In our sample, several stars have the YSOs' SED features as: Class I (approximately flat or rising SED into mid-IR ( $\alpha_{\text{IR}} > 0$ )) and Class II (falling SED into mid-IR ( $-1.5 < \alpha_{\text{IR}} < 0$ )). Class I YSOs are typically younger and possess more massive disks than Class II objects. In principle, YSOs should have been removed from our selection of MS stars using the H-R diagram. However, stars would cross the MS belt on the H-R diagram when they evolve from pre-main-sequence (PMS) to the zero-age main sequence (ZAMS) stars. Most of these stars are very close to ZAMS, and only a small fraction may have massive planetary disks. According to our SED fitting, we reject 20 YSOs in total and list them in the Table 1. In addition, we also purge another 3 stars (HIP 53911, HIP 77542, HIP 23633) classified as YSOs in SIMBAD although their IR slope

does not meet above criterion. All these rejected stars are listed in Table 1. We retain a sample of 79 stars.

In order to assess whether there is an excess IR emission in the rest of the sample, we calculate the significance of the excess to the stellar photospheric emission model in each *AKARI/FIS* band using following formula (Beichman et al. 2006; Moór et al. 2006):

$$\chi = [F_{IR} - F_{phot}]/\sigma_{IR} \quad (3)$$

where  $F_{IR}$  is the measured flux density;  $F_{phot}$  is the predicted photospheric flux density; and  $\sigma_{IR}$  is the uncertainty of the measured flux density. An object is considered as an excess candidate star when  $\chi > 3.0$  (Su et al 2006) in one or more of 65, 90, 140 or 160  $\mu\text{m}$  bands. Applying this criterion, we identify in total 75 FIR excess stars in the *AKARI/FIS* database. Due to the shallow *AKARI/FIS* flux limit, only 4 of the Hipparcos stars were sufficiently bright to have their photospheres detected in the far-IR in the absence of a FIR excess. Among these 75 stars, 72 stars have high quality 90  $\mu\text{m}$  flux densities ( $f_{qual} = 3$ ). The other three were flagged as having unreliable 90  $\mu\text{m}$  fluxes. Two of them are safely detected in 140  $\mu\text{m}$  or 160  $\mu\text{m}$  bands, indicating the presence of a cold disk; and the third has reliable fluxes in both 65 and 140  $\mu\text{m}$  and is a well known bright debris source.

The MIR excesses from WISE 22  $\mu\text{m}$  and 12  $\mu\text{m}$  are estimated in the same way. Among the 75 objects, 53 stars show excesses in the 22  $\mu\text{m}$  band at more than  $3\sigma$  level (see Figure 3b) after considering the systematical uncertainty of **0.13** mag (§2.2). 37 stars show excesses in the 12  $\mu\text{m}$  band after considering the systematical uncertainty of **0.06** mag. The *WISE* magnitudes for these 75 objects are presented in Table 2.

### 3. Properties of Debris Disks and Host Stars

We have identified a sample of 75 stars with debris disks. In this section, we will study the properties of host stars and debris disks. The stellar properties include magnitude, color, location on the H-R diagram as well as those derived from the SED fitting in the previous section. The properties of debris disks are derived by using the parameters obtained in modeling the IR excesses in *AKARI/FIS* and *WISE* data.

Previous studies suggested that debris disks are optically thin and usually consist of a narrow ring (Backman & Paresce 1993) in thermal equilibrium with the stellar radiation field. Therefore the IR excess is usually modeled as a single temperature blackbody (Kim et al. 2005; Bryden et al. 2006; Rhee et al. 2007). There are two free parameters in the fit, blackbody temperature and its normalization. To fully determine the model parameters, excesses in at least two bands are needed, while with more data points, we can get a



best fit by minimizing  $\chi^2$ . Therefore, according to the number of bands with detected FIR and MIR excesses (*AKARI/FIS* 4 bands and *WISE* 12  $\mu\text{m}$  and 22  $\mu\text{m}$ ), we further divide the IR excess sample into two groups: IR excess in a single band (Group I) and excesses in two or more bands (Group II). Note both Group I and II should show excess in at least one *AKARI/FIS* band. Only for sources in Group II can the dust temperature be fully determined for the single temperature dust model, while in Group I, by combining *AKARI/FIS* data with the upper limits at the *WISE* 22  $\mu\text{m}$ , we can derive an upper limit on the dust temperature. Among 75 debris disk candidates, the majority (55)<sup>4</sup> are in the Group II. In passing, we note that 11 objects are detected in two or more *AKARI/FIS* bands. They are brighter at 90  $\mu\text{m}$  on average, and a significant fraction (9/11) of these sources does display MIR excess. Similarly, bright sources are more likely to show 22  $\mu\text{m}$  excesses.

### 3.1. Stellar Properties of Debris Disk Hosts

It is evident that the debris stars do not evenly sample its parent Hipparcos stars, but are biased to early type stars, consistent with previous study (Rhee et al. 2007). It is puzzling that these stars are not particularly close to the lines of ZAMS, while previous studies suggested that incidence of debris disk decreases with the increase of the stellar age. The discrepancy may be caused by three factors, the contamination of PMS stars, large errors in the parallax measurements and large interstellar reddening. Since PMS stars have been excluded from the sample, so only the latter two possibilities need to consider. If we only include these sources with accuracy in the parallax measurement to 10%, most sources tend to distribute near the ZAMS (blue plus in Figure 1), suggesting that the discrepancy is attributed at least in part to the inaccuracy of the distance estimate. However, the rule of dust extinction cannot be ruled out because both the extinction and uncertainty of parallax increase with the distance of stars thus are likely correlated.

### 3.2. Disk Properties

By fitting the IR excess flux densities, we will derive the dust temperature and the fraction of the stellar luminosity reprocessed by dust. By combining with additional stellar parameters, we can estimate the dust location and other quantities. The inferred basic disk properties are listed in Table 3. In the following subsections, we will describe the method

---

<sup>4</sup>53 stars with 22  $\mu\text{m}$  excess and 2 stars without 22  $\mu\text{m}$  excess but with two or more *AKARI/FIS* band excesses.

and results in detail.

### 3.2.1. Dust Temperature

We fit the excessive flux densities in the *AKARI/FIS* and *WISE* bands with a single temperature blackbody model as described, convolved with the response functions of the corresponding filters. In the case of single band excess (Group I, 20 star in total), we derive a maximum temperature by combining the excess *AKARI/FIS* flux with the upper limits at 22  $\mu\text{m}$ , and the normalization of blackbody radiation at the maximum temperature. Note that this normalization is usually higher than the one assuming that the blackbody peaks at the detected IR band, as has been made in Rhee et al. (2007). In the case of two band excesses, we can fit the blackbody solution directly to determine the temperature and normalization. We estimate the uncertainty of a parameter by using  $\chi^2$  as a function of the parameter. We adopt  $\Delta\chi^2 = 2.7$  in the error estimate, i.e. at 90% confidence level for one interesting parameter. In the case of more than two band excesses (38 objects including 37 stars with 12  $\mu\text{m}$  excess; 30 stars have three band excesses and 8 stars have four or more band excesses), the best fit parameters are determined by minimizing  $\chi^2$ , and again the uncertainties of parameters are given at  $\Delta\chi^2 = 2.7$ . The typical uncertainty in the dust temperature is about 3 K. We do not use *IRAS* fluxes because these fluxes may suffer from contaminations, in particular for the objects beyond 100 parsecs, where the contamination of cirrus is severe due to poor spatial resolution of *IRAS*.

In most cases, a single temperature blackbody usually gives an acceptable fit to the data for sources with multi-band excesses. Examples of SED fitting are shown in Figure 4. We consider minimum  $\chi^2 > 6.7$  for three band excesses and  $\chi^2 > 9.2$  for four band excesses to be unacceptable (at  $< 1\%$  probability). Using these criteria, 15 stars require a more complicated model including 11 stars with excesses in three bands and 4 stars with excesses in four or more bands. This indicates either multi-temperature components or a non-blackbody nature of the dust grains. We use a double blackbody model to fit the SED of the four stars with excesses in four or more bands (Figure 5). The temperatures for the two components are (206, 54) K, (110, 41) K, (107, 45) K and (105, 37) K, respectively. Three of them are clustered around (100, 40) K, and the other ( $\sim 200$ , 50) K. The star with a warm component ( $\sim 200$  K) has a fairly large ratio of excesses in *W3* and *W4*, so the presence of warm component is independent of modeling, while other three show rather steep spectrum between *W3* and *W4*. The temperature of the warm component is similar to that of grains in the asteroid belt of our solar system, and while the cold component in the Kuiper belt. For 14 stars with three band excesses that cannot be well fitted by a single blackbody model, it

is insufficient to constrain the temperatures in a dual blackbody model. However, according to the excess flux ratio between W3 and W4, we speculate that about 7 stars may have a warm component.

Note weak 12  $\mu\text{m}$  excess does not significantly affect the fit to the cold component. Therefore, we will focus only on the cold component in the rest of this paper. The best fitted  $T_{\text{d}}$  is listed in column (6) in Table 3. The distribution of  $T_{\text{d}}$  is shown in Figure 6 (b). Dust temperatures are falling in the range of 27 to 194 K with a median value of 78 K. The dust temperatures of the disk correspond to the peak of blackbody emission from 26  $\mu\text{m}$  to 189  $\mu\text{m}$ .

### 3.2.2. Fractional Luminosity

Fractional luminosity  $f_{\text{d}}$  is defined as the ratio of IR luminosity of the debris disk to that of the star, frequently used to characterize the effective optical depth of the disk,

$$f_{\text{d}} = L_{\text{ir}}/L_{\star} \quad (4)$$

where  $L_{\text{ir}}$  is the IR luminosity estimated by the fitted IR blackbody model. The stellar luminosity  $L_{\star}$  is calculated from the best-fit Kurucz model. The uncertainties of  $f_{\text{d}}$  can be estimated by a combination of the uncertainties in the temperatures  $\sigma_{T_{\text{d}}}$  and normalization. The typical uncertainty of  $f_{\text{d}}$  is 0.14 for our sample.

We plot the distribution of the  $f_{\text{d}}$  in Figure 6(c). Our sample spends a large range of  $f_{\text{d}}$ ,  $1.04 \times 10^{-5} < f_{\text{d}} < 0.06$ , with a median value of  $1.18 \times 10^{-3}$ . Limited by the sensitivity of the *AKARI/FIS*, the distribution itself should not be taken too seriously because disks with low  $f_{\text{d}}$  can be detected by *AKARI/FIS* only for very bright nearby stars, resulting a distribution strongly biased to the higher  $f_{\text{d}}$ .

### 3.2.3. Dust location, Dust mass

With the assumption that the debris disk is optically thin in thermal equilibrium with the stellar radiation field, the temperature of a dust grain with a given chemical composition and grain size depends on the radial distance to the central star only (Kim et al. 2005). Assuming that the dust is located in a narrow ring between  $R - dR$  and  $R + dR$ , one can write the radius of dust ring  $R$  by the following formula (Backman & Paresce 1993):

$$R_{\text{d}} = (278/T_{\text{d}})^2(L_{\star}/L_{\odot})^{0.5} \quad (5)$$

Because this formula assumes that the dust is blackbody-like, the resulting  $R_d$  corresponds to a minimum possible radius (Moór et al. 2011). The uncertainties of  $R_d$  are estimated from the error propagation of the uncertainties of temperatures  $\sigma_{T_d}$ . This gives typical error of 10% in  $R_d$  formally. Figure 6 (d) shows the distribution of the dust location  $R_d$ .

The total mass  $M$  of dust can be written by the following formula (Rhee et al. 2007):

$$M_d = (4\pi a^3/3)\rho N \quad (6)$$

where  $N$  is the total number of grains in the disk,  $a$  and  $\rho$  are the mass weighted average radius and density of grains. For an optically thin dusty ring/shell of characteristic radius  $R$ ,

$$f_d = N\pi a^2/(4\pi R_d^2). \quad (7)$$

Then,

$$f_d/M_d \propto 1/(\rho a R_d^2). \quad (8)$$

If the characteristic grain size and density do not vary much in different debris disks, then one expects  $f_d/M_d$  to vary as the inverse square power of the disk radius,  $R_d$  (Rhee et al. 2007). The slope is a constant, which can be derived from the disks that their masses were derived from sub-millimeter data. We use the slope from Rhee et al. (2007) (see Figure 5). So we can change the equation to the following form:

$$M_d = f_d(R_d^2/9.12)M_\oplus. \quad (9)$$

where,  $f_d$  and  $R_d$  are taken from Table 3 in column (9) and column (7) respectively. Then the calculated dust mass is listed in column (8) in Table 3. Noting that we have adopted several assumptions in deriving dust mass, that are only valid statistically, thus the dust mass is only a rough estimate for individual object.

#### 4. Discussion

An effective way of characterizing the sample is to make a comparison with other sample in literature. A similar one is the *IRAS* debris disk sample, which was constructed by cross correlating the *Hipparcos* MS star catalog with the *IRAS* Point Source Catalog (PSC) and Faint Source Catalog (FSC) (Rhee et al. 2007). The sample consists of 146 stars within 120 pc of the Earth that show excess emissions at 60  $\mu\text{m}$ . The distance limit is so set to avoid possible heavy contamination arising from interstellar cirrus or star-forming regions. Most of these stars belong to early types, from late B to early K-type stars, similar to our sample. Despite the similar sensitivity of *IRAS* at 60  $\mu\text{m}$  band and *AKARI/FIS* at 90  $\mu\text{m}$ , only

27 stars in Rhee et al. are in common with ours, while 35 stars in total are within 120 pc in our sample.

To understand what causes the difference, we search the flux density at 60  $\mu\text{m}$  of Rhee’s sample from the *IRAS* PSC and FSC with a matching radius of 45'' as described in Rhee et al. (2007) Figure 7 shows that *IRAS* flux at 60 $\mu\text{m}$  and *AKARI* flux at 90 $\mu\text{m}$  are fairly well correlated for these detected in both bands (29 in total including 27 in our sample and 2 PMS stars rejected from our sample mentioned in §2.3) and within 120 parsecs of the Earth. A logarithm linear fit to the data yields a best fit  $\log f_{90\mu\text{m}} = 0.90 \log f_{60\mu\text{m}} - 0.08$ . The ratio of the two fluxes is certainly dependent on the disk temperature, but with only 29 data points in hand, we will not explore this further. In our sample, 27 stars beyond 120 parsecs have *IRAS* detection. For these stars, the flux ratios between *IRAS* 60  $\mu\text{m}$  and that of *AKARI/FIS* 90  $\mu\text{m}$  are substantially higher than those of nearby stars, especially for sources with  $f_{60\mu\text{m}} > 1$  Jy. This is likely caused by source contamination in *IRAS*. With a factor of more than four improvement in the spatial resolution, the contamination is greatly reduced in *AKARI/FIS* flux.

We examine these sources that appear only in one sample in detail. 9 stars within 120 parsecs are included in our sample but not in Rhee et al. (2007). 5 of them (HIP 10064, HIP 20884, HIP 26062, HIP 48613, HIP 57757) have *IRAS* detections. HIP 57757 was rejected by Rhee as a non-IR excess star. 4 stars are not in the rejected source table of Rhee et al. HIP 20884 and HIP 26062 were excluded due to the spectral type cut in Rhee et al. HIP 10064 and HIP 48613 were reported to show a FIR excess (Oudmaijer 1992; Chen et al. 2006). While the rest 4 of them (HIP 65875, HIP 77441, HIP 88983, HIP 90491) do not have available *IRAS* data. The *AKARI/FIS* 90  $\mu\text{m}$  flux densities of these 4 stars are in the range from 0.4 to 0.7Jy. Adopting above relation between 90 and 60  $\mu\text{m}$  relation for sources in common, 60  $\mu\text{m}$  flux is expected to be 0.4-0.8 Jy. HIP 88983 and HIP 90491 are in “*IRAS* Faint Source Catalog Rejects” with a 60  $\mu\text{m}$  flux of 0.33 Jy and 0.28 Jy with  $f_{\text{qual}} = 2$  and 1, respectively. This suggests that these sources have fainter 60  $\mu\text{m}$  flux than expected, which indicates cool debris disks. To produce a flux ratio of 0.6 between 60 to 90  $\mu\text{m}$ , the blackbody temperature would be about 50K. At this temperature, flux ratios of 140 and 160 to 90  $\mu\text{m}$  are about 0.9 and 0.7, so the expected 140 and 160  $\mu\text{m}$  flux is below the detection limits in both bands, consistent with none detections in either band. The other two stars may have similar situations. Note two of debris disk candidates in the sample that have a firm flux only at 140 or 160  $\mu\text{m}$  are likely even cooler.

On the other hands, most sources (119/146) in Rhee’s sample are not in ours. Most of these sources (113/119) have a flux  $f_{60\mu\text{m}} < 0.63\text{Jy}$ , and it is not surprise that they are undetected by *AKARI/FIS*(red dots in Figure 7). According to the relation between  $f_{90}$

and  $f_{60}$ , we expect  $f_{90\mu\text{m}} < 0.55\text{Jy}$ , which is below the formal flux limit of the AKARI. Thus undetected of these sources may be entirely due to shallowness of the *AKARI/FIS* survey. 6 bright *IRAS* stars are not in our final sample. Among them, the two brightest stars (HIP 53911 and HIP 77542) are actually detected by *AKARI/FIS* but rejected as PMS according to SIMBAD classification. We checked the other four stars and found no matching sources in *AKARI/FIS* catalog even at a larger matching radius.

For comparison, we over-plot the disk parameters of IRAS sample (Table 2 of Rhee et al. 2007) in Figure 6(b),(c),(d). Only sources with a fitted temperature, i.e., detected in more than one *IRAS* band, are shown. Our sample distributes in a relatively narrower temperature range than the *IRAS* sample. However, as we have discussed above that 4 stars in our sample without available *IRAS* data may have very low temperature, then this difference of temperature distribution between two sample may be not real. Our sample tends to have larger excesses and to possess more distant disks due to the different flux limits and the distance cut used in selection of the sample.

A caution should be given here that both dust temperature and normalization in Rhee et al. (2007) is based on solely *IRAS*, which have much poorer sensitivity in the MIR in comparison with *WISE*. Therefore, the dust temperature for a large fraction of objects in their sample could not be determined, and was artificially assigned to 85 K so the peak emission is at 60  $\mu\text{m}$ . Even for those objects with multi-bands *IRAS* detections, the dust temperatures were less well determined than in this paper.

Finally, a total of 43 stars were already reported in literature (notes in Table 3), so 32 stars are reported to have infrared excesses for the first time in this paper. Most of them locates at a distance more than 120 parsecs from the Earth, but are relatively very luminous. As Kalas et al. (2002) pointed out: “Pleiades-like dust detected around the star is capable of producing the FIR emission rather than the Vega phenomenon”. HIP 78594 (Table 1, marked with ‘a’) which was rejected by Moór et al. (2006), is such a kind of star. So these 32 new IR excess stars need to be further checked out by coronagraphic optical observations to confirm whether debris disks are response for the infrared excesses.

## 5. Summary

In this paper we cross-correlate the AKARIBSC with the *Hipparcos* MS star catalog using a matching radius adapted to the local stellar surface density and yield a sample 136 far-infrared detected stars (at  $> 90\%$  reliability) at least in one band. After rejecting 57 stars classified as young stellar objects, PMS stars and other type stars with known dust

disks or with potential contaminations, we obtain a sample of **75** candidate stars with debris disks and 4 stars without FIR excess. The stars in the sample spans from B to K-types, with only 2 G-type and 1 K-type stars.

With the shallow limit of *AKARI/FIS*, the survey can only recover the brightest debris disks. This represents a unique sample of luminous debris disks that are derived uniformly from an all sky survey with a spatial resolution a factor of two better than the previous survey by *IRAS*. This sample is also complementary to the deep, small area surveys or deep surveys of nearby stars as already carried out with *Spitzer* and *ISO* that find out mostly faint debris systems. Moreover, by collecting the IR photometric data from other public archives, 55 stars have IR excesses in more than one band, allowing an estimate of the dust temperature. We fit a blackbody model to the broad band SEDs of these stars to derive the statistical distribution of the disk parameters. 4 objects with four or more band excesses can be fitted by a double blackbody model. Three of them are clustered around (100, 40) K, and the other ( $\sim$ 200, 50) K.

We are grateful to the anonymous referee for his/ her comments that improved the paper. This work is based on observations with *AKARI*, a JAXA project with the participation of ESA and makes use of data products from *Hipparcos* Catalogs ( the primary result of the Hipparcos space astrometry mission, undertaken by the European Space Agency), *2MASS* (a joint project of the University of Massachusetts and the Infrared Processing and Analysis Center /California Institute of Technology), *WISE* (a joint project of the University of California, Los Angeles, and the Jet Propulsion Laboratory/California Institute of Technology). This work makes use of the NASA/IPAC Infrared Science Archive, which is operated by the Jet Propulsion Laboratory, California Institute of Technology, under contract with the National Aeronautics and Space Administration. This research makes use of ATLAS9 model and the SIMBAD database, operated at the CDS, Strasbourg, France.

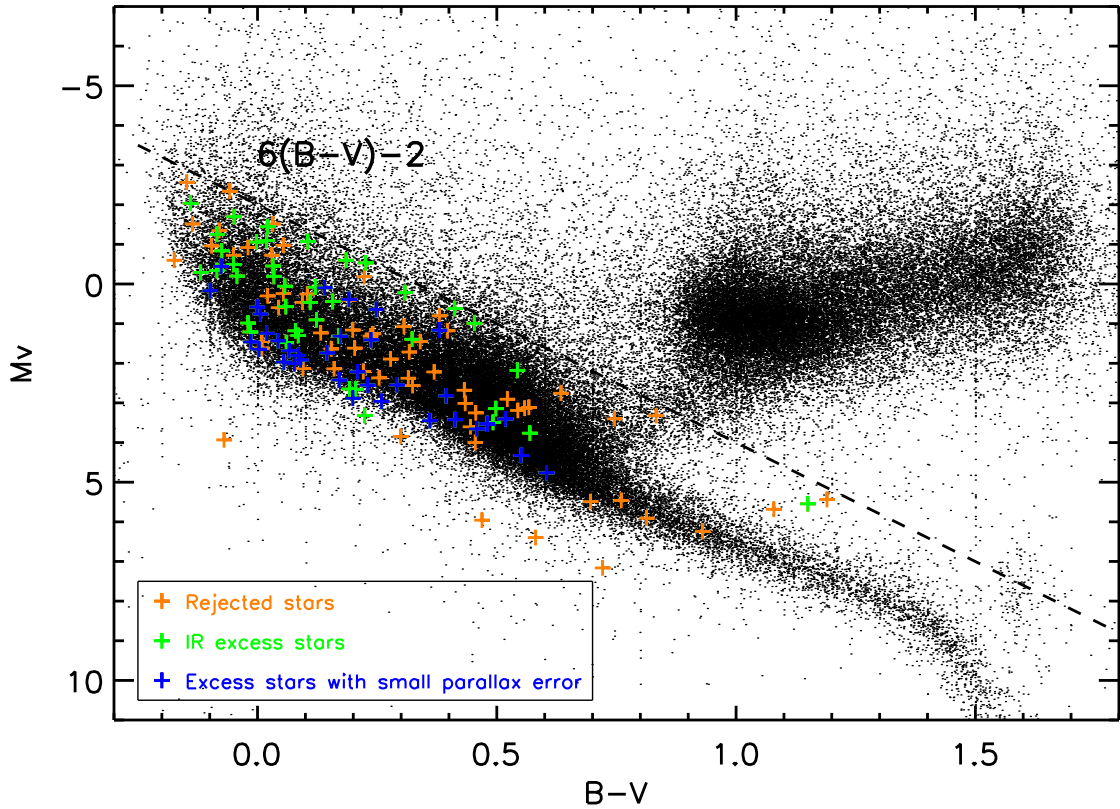


Fig. 1.— Selection of main sequence (MS) stars on H-R diagram of the *Hipparcos* field stars. The stars below the dashed line are MS stars, which have been searched for far-infrared excess emission using *AKARI/FIS*. The FIR excessive stars are plotted with a plus: green and blue plus represent for the debris disk candidates, blue plus for the source with an accuracy in the parallax measurement to 10%, orange plus for the rejected source.



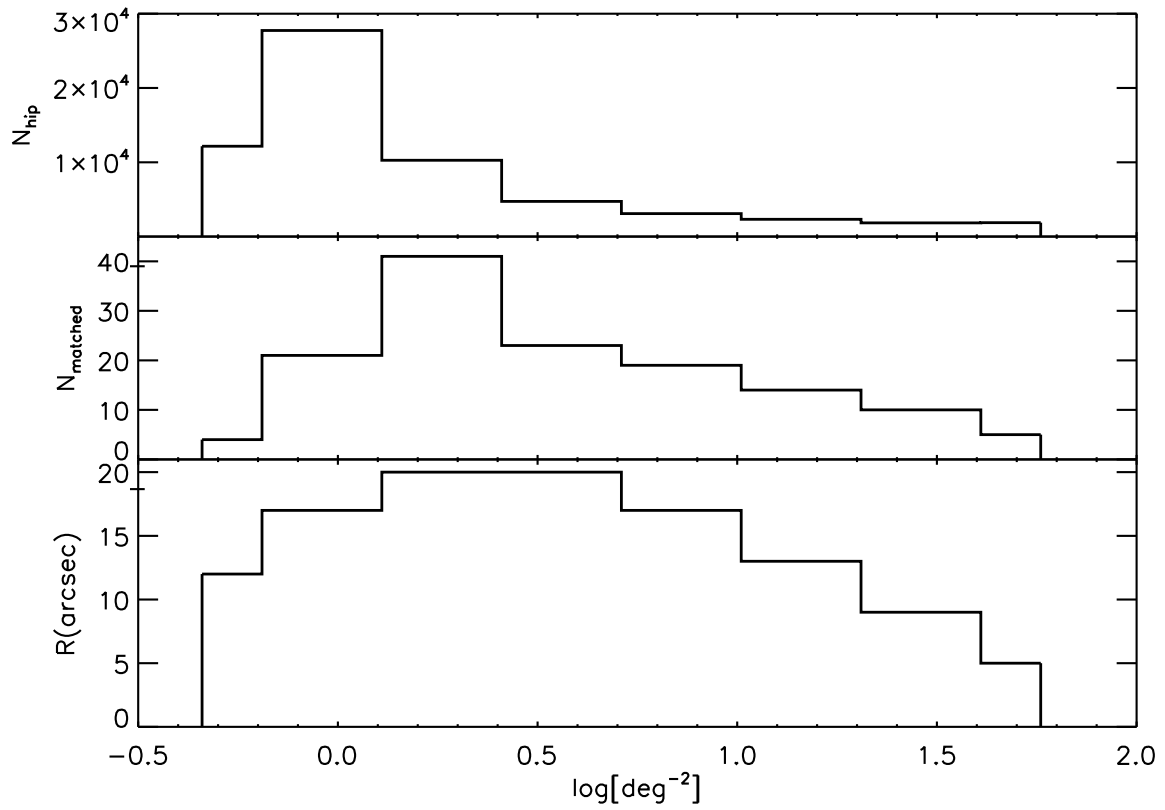


Fig. 2.— The *AKARI/FIS* local surface density distribution of the *Hipparcos* MS stars and the corresponding matching radius and matched numbers.

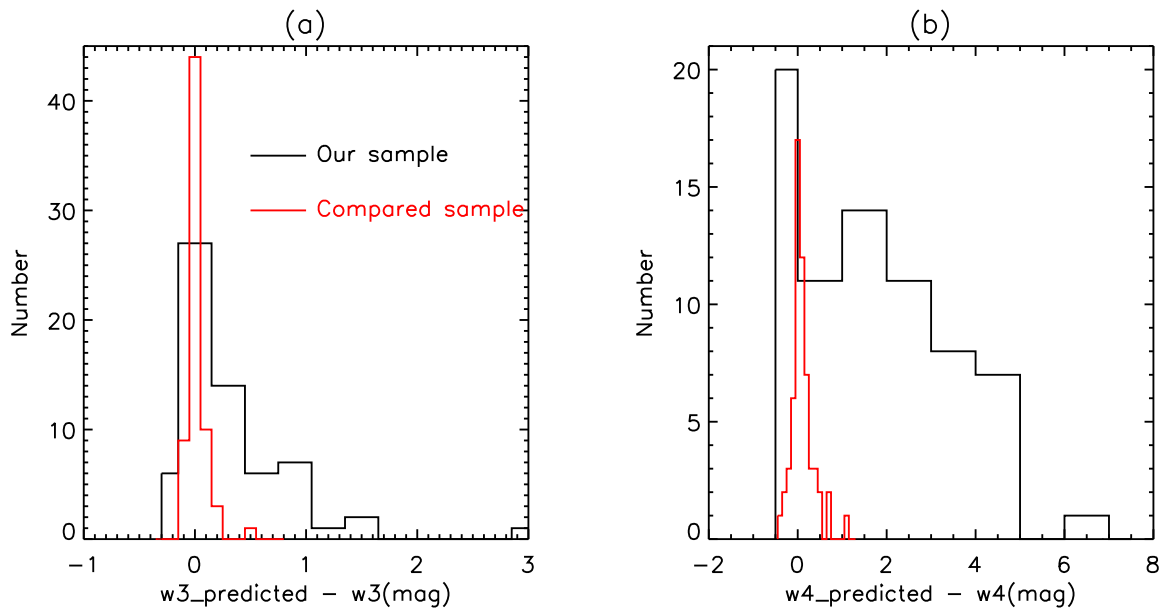


Fig. 3.— The distribution of the difference between the observed magnitude in *WISE* *W3* and *W4* bands and the predicted stellar photosphere model. The black line represents for our final sample. The red line is for the matched random sample as described §2.2.

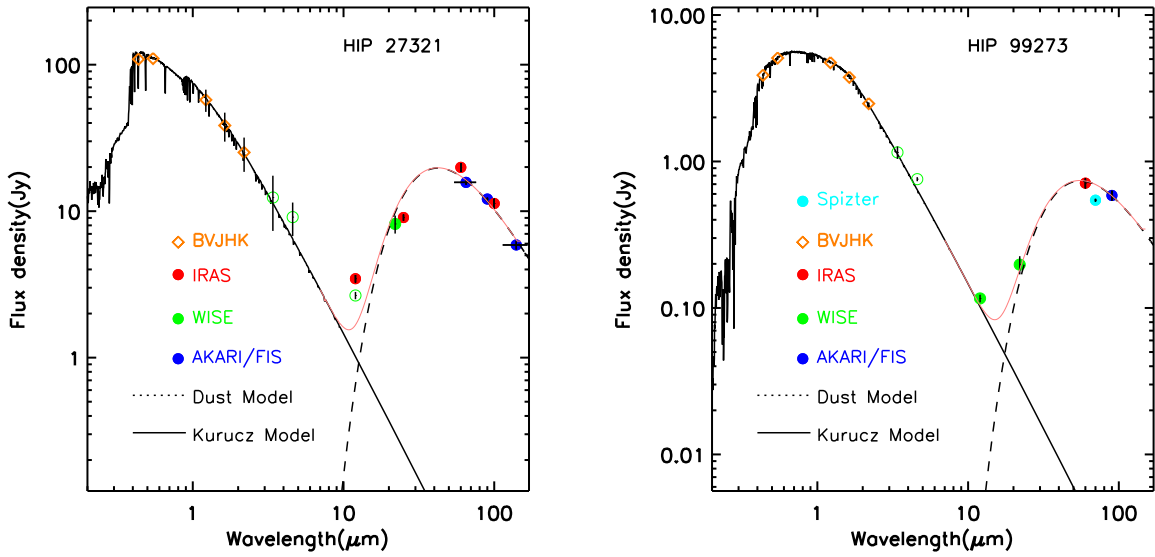


Fig. 4.— SEDs for IR excess stars in our sample. The photospheric models and the disk models are shown as solid black lines and dotted lines, respectively. The different symbols represent the different data-sets - orange diamonds: *BVJHK*, red filled dots: *IRAS*, blue filled dots: *AKARI/FIS*, cyan filled dots: *Spitzer*, green filled dots: *WISE* without saturations, green hollow circles: *WISE* with saturations.

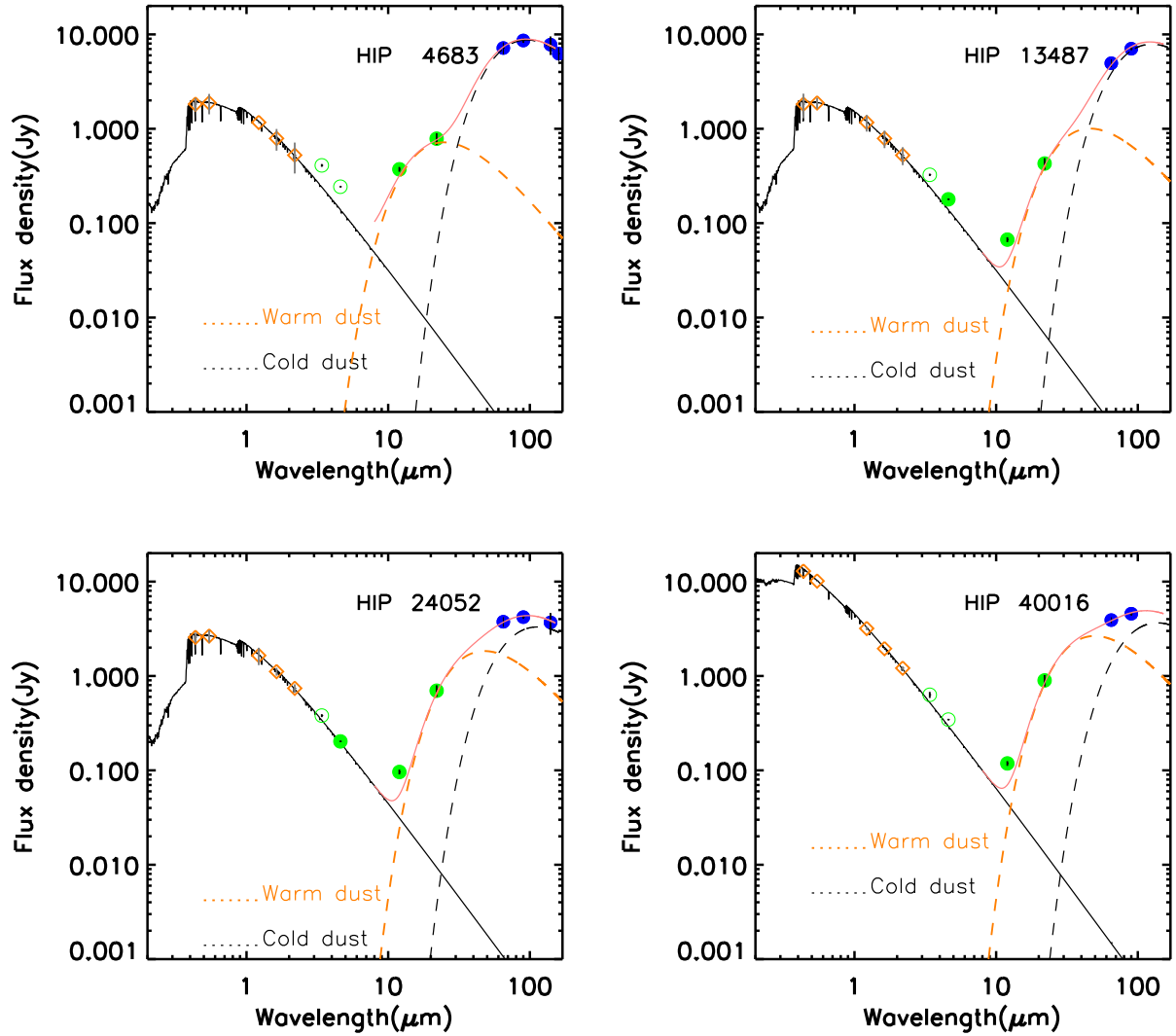


Fig. 5.— SED fittings of the 4 stars that require double blackbody components. The symbols legend as Figure 4. The orange dotted line is the fitted blackbody emission of the warm dust.

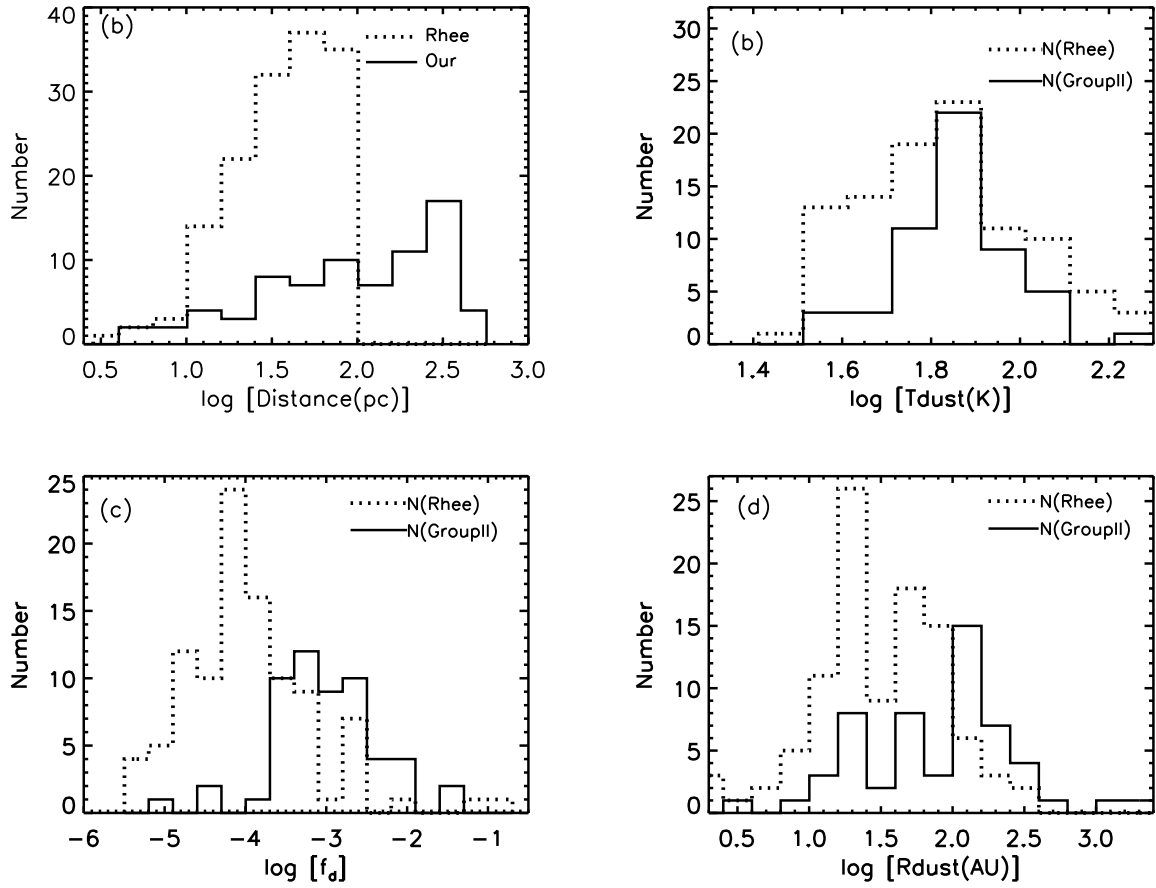


Fig. 6.— The distributions of disk parameters for IR excess stars. Only Group II objects were plotted in the panel b, c, d. The black solid line is our sample. The added dotted line is the *IRAS* sample (Rhee et al. 2007).

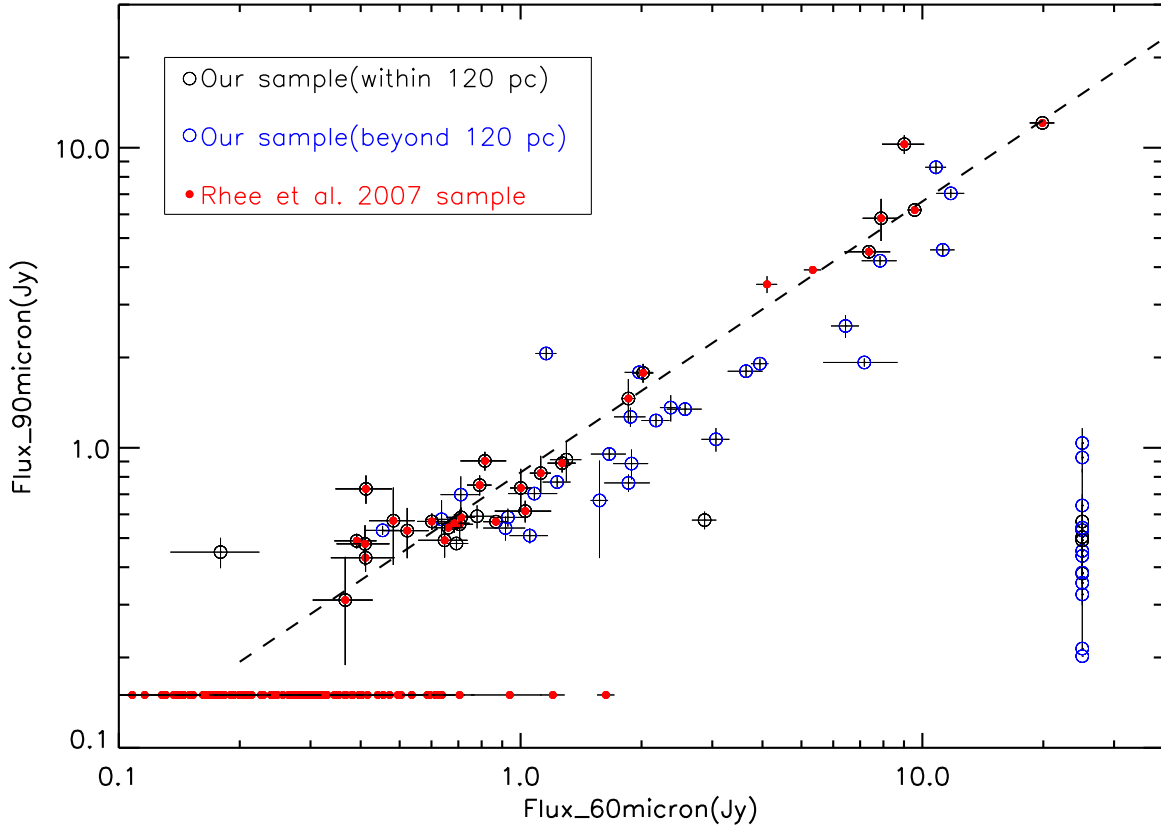


Fig. 7.— A comparison of flux densities at  $90\ \mu\text{m}$  from *AKARI/FIS* and  $60\ \mu\text{m}$  flux from *IRAS*. The hollow circles are our sample stars: black— within 120 parsecs; blue— beyond 120 parsecs. The red dots are Rhee’s sample. Our sample stars without *IRAS* detections are plotted on the right hand edge and Rhee’s sample stars without *AKARI/FIS* detections are plotted on the downward edge.

Table 1. The list of rejected sources

HIP	<i>AKARI/FIS</i> identification	Reason for Rejection
3401	0043182+615442	1
4023 <sup>a</sup>	0051337+513424	4
5147	0105535+655820	2
13330 <sup>a</sup>	0251319+674845	4
15984 <sup>a</sup>	0325506+305559	4
16826	0336292+481134	2
17890	0349363+385902	3
19395 <sup>a</sup>	0409164+304638	4
19720 <sup>a</sup>	0413352+101240	4
19762 <sup>b</sup>	0414129+281229	4
22910	0455460+303320	3
22925	0455593+303403	3
23143	0458465+295039	3
23428	0502065-712018	1
23633	0504502+264318	3
23734	0506086+585829	2
23873	0507494+302410	3
24552	0516006-094831	3
25253	0524009+245746	3
25258	0524079+022751	3
25299	0524426+014349	3
25793	0530272+251957	3
26295	0535587+244500	3
26451	0537385+210834	2
28582	0601597+163102	2
30089	0619582-103822	5
30800	0628177-130310	2
32349	0645085-164258	8
32677 <sup>a</sup>	0648585-150849	4
32923	0651333-065751	2
36369	0729106+205450	1
37279	0739178+051322	8
53691	1059071-770138	3
53911	1101516-344214	3
54413	1108017-773912	3
56379	1133251-701146	2
58520	1200066-781135	2
60936	1229071+020309	6
63973 <sup>b</sup>	1306360-494107	4
71352	1435303-420930	1
72685 <sup>b</sup>	1451400-305312	4
77542	1549578-035515	3
77952 <sup>b</sup>	1555094-632558	4
78034	1556019-660907	2
78317	1559283-402150	3
78594 <sup>a</sup>	1602491-044922	4

Table 1—Continued

HIP	<i>AKARI/FIS</i> identification	Reason for Rejection
78943 <sup>b</sup>	1606579-274308	4
79080	1608344-390612	3
79476	1613116-222904	3
81624	1640176-235344	3
82747	1654450-365317	3
85792	1731503-495235	2
93975 <sup>b</sup>	1908039+214151	4
94260	1911115+154717	3
97649	1950472+085209	8
101983	2040025-603307	8
104580	2111024-634106	7
105638	2123489-404203	1
106079	2129147+442027	2
111785	2238316+555006	2
112377 <sup>b</sup>	2245378+415308	4

Note. — a: Stars in nebula.

b: Rejected by diffuse WISE images.

Col.(1): *Hipparcos* identification. Col.(2): *AKARI/FIS* identification. Col.(3): Reason for rejection. 1. O star. 2. Be star. 3. Young stellar objects (YSOs) or PMS stars. 4. Contamination. 5. Post AGB star. 6. Quasar. 7. *AKARI/FIS* flux density is not reliable (F<sub>qual</sub>=1). 8. No FIR excess.



Table 2. The photometry and flux density for all sources

Name	Hipparcos		2MASS			WISE									AKARI/FIS					
	HIP	B mag	V mag	J mag	H mag	K mag	rdflg	w1 mag	w2 mag	w3 mag	w4 mag	w1sat %	w2sat %	w3sat %	w4sat %	65 $\mu$ m Jy	90 $\mu$ m Jy	140 $\mu$ m Jy	160 $\mu$ m Jy	FQUAL
746	2.61	2.27	1.71	1.58	1.45	333	-0.88	-0.18	1.46	1.33	0.22	0.19	0.24	0.00	0.26	0.73	0.35	0.05	1311	3.1
4683	8.65	8.60	7.87	7.55	7.45	111	7.19	7.12	4.73	2.56	0.07	0.00	0.00	0.00	7.17	8.61	7.78	6.26	3333	3.8
4789	6.70	6.70	6.53	6.56	6.55	111	6.52	6.47	5.68	3.17	0.14	0.06	0.00	0.00	1.15	1.23	null	0.57	1311	11.1
7345	5.69	5.62	5.49	5.53	5.46	111	5.47	5.30	5.34	3.74	0.19	0.14	0.00	0.00	1.92	1.78	2.35	0.03	1311	2.7
7978	6.08	5.54	4.79	4.40	4.34	333	4.17	3.91	4.22	3.95	0.21	0.22	0.00	0.00	1.44	0.90	0.56	null	1311	7.0
8851	9.58	9.40	8.99	8.98	8.95	122	8.91	8.93	8.35	6.11	0.01	0.00	0.00	0.00	0.32	0.53	1.50	null	1311	8.4
10064	3.14	3.00	2.74	2.77	2.68	333	1.46	1.25	2.68	2.46	0.20	0.19	0.09	0.00	0.42	0.59	null	null	1311	4.3
10670	4.03	4.01	3.80	3.86	3.96	331	3.95	3.64	3.99	3.51	0.19	0.19	0.00	0.00	1.10	0.75	null	0.49	1311	6.2
11847	7.87	7.47	6.70	6.61	6.55	111	6.54	6.52	6.50	4.24	0.14	0.06	0.00	0.00	0.72	0.57	null	null	1311	5.2
13487	8.84	8.45	7.66	7.61	7.57	111	7.44	7.45	6.59	3.22	0.06	0.00	0.00	0.00	4.95	7.05	3.08	3.60	3311	5.3
14043	5.19	5.24	5.32	5.40	5.43	111	5.33	5.26	5.36	4.01	0.22	0.15	0.00	0.00	0.62	1.04	1.90	4.71	1311	14.8
16188	7.39	7.30	6.56	6.55	6.49	111	6.47	6.41	6.32	5.27	0.13	0.06	0.00	0.00	1.54	0.76	0.89	1.39	1311	18.3
17812	8.56	8.45	8.07	8.08	8.00	111	8.02	8.00	7.56	5.50	0.00	0.00	0.00	0.00	0.45	0.45	0.02	1.45	1311	8.3
17941	8.93	8.81	8.60	8.62	8.58	122	8.58	8.58	7.50	4.24	0.00	0.00	0.00	0.00	1.02	1.36	2.04	1.54	1311	12.2
19475	9.57	9.30	8.06	8.01	7.94	111	7.88	7.90	7.93	7.93	0.03	0.00	0.00	0.00	null	0.20	null	4.02	1113	9.4
20556	7.02	6.84	6.31	6.24	6.26	111	6.26	6.15	5.97	4.78	0.14	0.09	0.00	0.00	0.25	0.77	0.55	0.12	1311	3.6
20884	5.44	5.54	5.73	5.79	5.79	111	5.87	5.75	5.50	3.07	0.18	0.12	0.00	0.00	null	0.57	null	0.57	1311	18.2
21219	7.06	6.90	6.52	6.52	6.48	111	6.45	6.44	6.50	6.43	0.13	0.06	0.00	0.00	null	0.21	1.93	null	1131	5.7
21898	8.52	8.20	8.02	7.99	7.89	111	7.82	7.82	7.35	5.36	0.05	0.00	0.00	0.00	0.97	0.95	1.11	1.49	1311	16.9
22845	4.73	4.64	4.85	4.52	4.42	311	4.41	4.17	4.43	4.06	0.23	0.23	0.00	0.00	0.23	0.43	0.64	3.41	1311	8.1
23451	8.61	8.50	7.69	7.62	7.59	111	7.59	7.63	6.92	3.95	0.12	0.00	0.00	0.00	null	0.82	null	null	1311	4.0
24052	8.23	8.10	7.28	7.35	7.30	111	7.27	7.31	6.20	2.69	0.08	0.00	0.00	0.00	3.75	4.20	3.70	0.93	3331	9.9
26062	7.00	6.97	6.84	6.92	6.82	111	6.81	6.75	5.13	2.29	0.11	0.04	0.00	0.00	1.44	0.91	null	1.29	1311	4.1
27296	7.14	7.12	7.09	7.13	7.12	111	7.10	7.14	6.71	3.91	0.09	0.00	0.00	0.00	0.87	1.35	1.34	0.83	1311	5.0
27321	4.02	3.85	3.67	3.54	3.53	333	3.48	3.18	2.60	0.01	0.24	0.24	0.09	0.00	15.72	12.10	5.88	2.95	3331	4.2
32345	7.44	7.45	7.50	7.53	7.52	111	7.47	7.51	7.30	5.96	0.06	0.00	0.00	0.00	0.64	0.59	2.18	0.66	1311	10.5
36437	7.10	7.18	7.30	7.43	7.38	111	7.33	7.43	7.02	3.68	0.08	0.00	0.00	0.00	0.70	0.64	0.00	null	1311	11.2
36581	8.12	7.95	7.82	7.77	7.69	111	7.76	7.60	6.49	4.70	0.05	0.00	0.00	0.00	0.94	0.53	null	1.55	1311	7.7
40016	6.32	6.47	6.72	6.84	6.83	111	6.71	6.74	5.97	2.41	0.13	0.03	0.00	0.00	3.91	4.57	2.15	0.68	3311	3.5
40024	7.85	7.93	8.04	8.06	8.06	111	8.05	8.05	7.37	4.05	0.00	0.00	0.00	0.00	1.30	1.78	1.22	1.24	1311	4.1
40748	10.38	10.40	10.32	10.31	10.25	222	10.15	9.95	8.57	5.72	0.00	0.00	0.00	0.00	0.22	0.44	null	null	1311	13.2
41650	8.60	8.60	8.43	8.28	7.92	111	7.04	6.30	3.09	1.13	0.24	0.15	0.08	0.00	1.41	1.27	1.48	0.23	1311	5.9
44001	5.87	5.66	5.27	5.21	5.16	111	5.16	4.98	5.20	4.89	0.21	0.18	0.00	0.00	0.17	0.49	null	1.48	1311	6.3

Table 2—Continued

Name	Hipparcos		2MASS			WISE										AKARI/FIS					
HIP	B	V	J	H	K	rdfkg	w1	w2	w3	w4	w1sat	w2sat	w3sat	w4sat	65 $\mu$ m	90 $\mu$ m	140 $\mu$ m	160 $\mu$ m	FQUAL	offset	
	mag	mag	mag	mag	mag		mag	mag	mag	mag	%	%	%	%	Jy	Jy	Jy	Jy		"	
45581	5.30	5.28	5.24	5.27	5.17	111	5.06	4.90	5.14	4.84	0.20	0.14	0.00	0.00	0.39	0.67	0.50	null	1311	11.8	
46021	8.98	8.90	8.62	8.66	8.59	112	8.53	8.53	7.59	5.50	0.00	0.00	0.00	0.00	null	0.58	1.93	1.22	1311	8.6	
48613	5.71	5.72	5.70	5.76	5.74	111	5.71	5.61	5.66	4.56	0.18	0.14	0.00	0.00	0.99	0.48	null	null	1311	18.3	
53524	7.60	7.36	6.91	6.87	6.79	111	6.72	6.75	6.69	5.47	0.10	0.02	0.00	0.00	0.62	0.57	1.29	0.20	1311	2.7	
55505	9.72	8.52	6.40	5.76	5.59	111	5.50	5.34	3.11	0.20	0.20	0.15	0.07	0.00	7.18	5.82	2.80	2.57	3311	8.5	
57632	2.23	2.14	1.85	1.93	1.88	333	0.46	0.13	2.06	1.70	0.24	0.23	0.24	0.00	0.38	0.61	0.22	2.20	1311	7.3	
57757	4.15	3.60	2.60	2.36	2.27	333	0.71	0.83	2.39	2.29	0.24	0.22	0.21	0.00	0.15	0.45	null	2.39	1311	15.8	
60074	7.63	7.03	5.87	5.61	5.54	111	5.52	5.36	5.54	5.18	0.18	0.13	0.00	0.00	0.62	0.56	null	null	1311	9.4	
61498	5.78	5.78	5.78	5.79	5.77	111	5.37	5.40	5.02	1.22	0.17	0.10	0.00	0.00	6.07	4.50	3.26	null	3311	8.9	
65875	8.58	8.08	7.17	6.97	6.90	111	6.86	6.86	6.70	3.99	0.20	0.00	0.00	0.00	0.31	0.57	null	null	1311	6.7	
73145	8.05	7.90	7.60	7.56	7.52	111	7.51	7.52	6.92	4.27	0.07	0.00	0.00	0.00	0.60	0.56	0.07	null	1311	5.4	
74421	6.02	6.01	5.91	5.91	5.91	111	5.91	5.81	5.82	5.26	0.17	0.11	0.00	0.01	0.81	2.06	4.51	5.28	1331	16.4	
76736	6.51	6.43	6.30	6.34	6.27	111	6.27	6.22	6.16	5.01	0.15	0.08	0.00	0.00	0.45	0.57	null	0.17	1311	10.4	
76829	5.04	4.62	4.02	3.73	3.80	333	3.68	3.09	3.65	3.52	0.25	0.23	0.02	0.00	1.23	0.54	null	1.71	1311	9.0	
77441	8.57	8.10	7.39	7.22	7.20	111	7.16	7.18	7.07	6.35	0.11	0.00	0.00	0.00	0.30	0.38	null	0.36	1311	5.7	
79977	9.58	9.09	8.06	7.85	7.80	111	7.76	7.76	7.46	4.29	0.08	0.00	0.00	0.00	0.63	0.70	null	1.04	1311	6.9	
80951	10.04	9.40	8.52	8.32	8.26	112	8.20	8.23	8.19	7.93	0.00	0.00	0.00	0.00	0.12	0.38	1.40	null	1311	6.9	
81474	6.84	6.70	5.90	5.78	5.69	111	5.61	5.50	5.45	3.79	0.20	0.12	0.00	0.00	1.70	1.92	null	0.06	1311	12.5	
81891	6.38	6.46	6.58	6.67	6.63	111	6.55	6.62	6.29	4.45	0.12	0.04	0.00	0.00	0.52	0.70	null	0.12	1311	8.5	
82770	8.46	7.95	6.96	6.75	6.64	111	6.61	6.59	6.67	6.54	0.14	0.04	0.00	0.00	0.58	0.35	0.60	null	1311	15.7	
83505	8.24	8.10	7.52	7.54	7.52	111	7.47	7.51	7.24	5.23	0.15	0.00	0.00	0.00	1.25	0.89	null	2.87	1311	4.0	
85537	5.62	5.39	4.81	4.88	4.80	111	4.78	4.57	4.80	4.60	0.22	0.22	0.00	0.00	0.16	0.31	null	null	1311	10.1	
86078	8.00	7.80	7.02	6.95	6.79	111	6.71	6.70	6.72	6.08	0.12	0.03	0.00	0.00	0.47	0.54	1.91	null	1311	19.1	
87108	3.79	3.75	3.59	3.66	3.62	333	3.68	3.36	3.65	3.12	0.26	0.24	0.03	0.00	1.31	0.89	null	0.59	1301	5.7	
87807	7.94	7.70	7.45	7.45	7.39	111	7.34	7.37	6.97	5.49	0.18	0.00	0.00	0.00	0.08	0.51	null	0.42	1311	6.0	
88399	7.46	7.01	6.16	6.02	5.91	111	5.76	5.70	5.80	4.94	0.18	0.10	0.00	0.00	0.60	0.49	0.45	null	1311	4.7	
88983	8.15	8.00	7.30	7.19	7.18	111	7.16	7.17	7.22	7.07	0.09	0.00	0.00	0.00	0.26	0.50	2.25	null	1311	18.3	
90491	8.76	8.50	8.23	8.21	8.13	111	8.09	8.10	7.97	6.12	0.00	0.00	0.00	0.00	null	0.49	1.03	0.51	1311	4.5	
91262	0.03	0.03	-0.18	-0.03	0.13	333	-2.03	-2.08	0.02	-0.16	0.31	0.31	0.30	0.00	6.58	6.20	4.05	3.22	3311	3.4	
92800	6.80	6.80	6.53	6.54	6.50	111	6.42	6.42	6.17	4.05	0.13	0.04	0.00	0.00	2.71	2.55	2.19	3.02	3311	6.4	
93000	7.37	7.15	6.63	6.61	6.58	111	6.54	6.46	6.05	4.16	0.13	0.05	0.00	0.00	1.17	1.80	0.78	null	1311	11.9	
95270	7.52	7.04	6.20	5.98	5.91	111	5.89	5.81	5.89	3.95	0.18	0.11	0.00	0.00	1.71	1.46	1.24	1.23	1311	7.9	
95619	5.64	5.66	5.67	5.66	5.68	111	5.68	5.56	5.61	4.58	0.21	0.13	0.00	0.00	0.45	0.73	0.07	null	1311	7.6	

Table 2—Continued

Name	Hipparcos		2MASS			WISE									AKARI/FIS					
HIP	B	V	J	H	K	rdfg	w1	w2	w3	w4	w1sat	w2sat	w3sat	w4sat	65 $\mu$ m	90 $\mu$ m	140 $\mu$ m	160 $\mu$ m	FQUAL	offset
	mag	mag	mag	mag	mag		mag	mag	mag	mag	%	%	%	%	Jy	Jy	Jy	Jy		"
99273	7.66	7.18	6.32	6.09	6.08	111	6.06	5.88	6.00	4.06	0.16	0.07	0.00	0.00	1.22	0.59	1.48	0.15	1311	14.6
101612	5.04	4.75	4.28	4.02	4.04	333	4.06	3.58	4.04	3.87	0.24	0.22	0.00	0.00	null	0.53	null	0.37	1311	4.9
102761	8.01	7.97	7.89	7.93	7.95	111	7.92	7.95	7.13	4.06	0.03	0.00	0.00	0.00	1.66	1.91	1.59	0.01	1311	11.0
104354	8.37	8.31	8.12	8.13	8.12	112	8.10	8.13	7.21	4.70	0.00	0.00	0.00	0.00	0.10	0.54	null	null	1311	7.3
111214	9.16	8.90	8.58	8.64	8.62	122	8.59	8.62	8.19	6.50	0.00	0.00	0.00	0.00	0.20	0.32	1.12	0.30	1311	12.8
111429	6.88	7.00	7.19	7.27	7.29	111	7.23	7.34	7.38	6.68	0.08	0.00	0.00	0.00	0.10	0.93	2.63	1.26	1311	15.2
113368	1.25	1.17	1.04	0.94	0.94	333	-1.47	-0.75	1.11	0.79	0.31	0.28	0.29	0.00	8.30	10.27	7.71	4.66	3131	4.9
114189	6.25	5.98	5.38	5.28	5.24	111	5.19	5.04	5.21	4.85	0.20	0.16	0.00	0.00	1.12	0.48	0.26	3.48	1311	4.8
118289	7.13	7.17	7.18	7.26	7.26	111	7.18	7.26	6.22	3.64	0.06	0.00	0.00	0.00	1.13	1.07	1.09	null	1311	6.3

Note. — Col.(1): *Hipparcos* identification. Col.(2): B magnitude. Col.(3): V magnitude. Col.(4): J magnitude. Col.(5): H magnitude. Col.(6): K magnitude. Col.(7): Col. Read flag. (8): *WISE* W1 magnitude. Col.(9): *WISE* W2 magnitude. Col.(10): *WISE* W3 magnitude. Col.(11): *WISE* W4 magnitude. Col.(12): Saturated pixel fraction, W1. Col.(13): Saturated pixel fraction, W2. Col.(14): Saturated pixel fraction, W3. Col.(15): Saturated pixel fraction, W4. Col.(16): *AKARI/FIS* 65  $\mu$ m flux density. Col.(17): *AKARI/FIS* 90  $\mu$ m flux density. Col.(18): *AKARI/FIS* 140  $\mu$ m flux density. Col.(19): *AKARI/FIS* 160  $\mu$ m flux density. Col.(20): Flux density quality flag in *AKARI/FIS* 4 bands: 3=High quality (the source is confirmed and flux is reliable); 2=The source is confirmed but flux is not reliable (see FLAGS); 1=The source is not confirmed; 0=Not observed (no scan data available). Col.(21): *AKARI/FIS* position offset.

Table 3. The star basic properties and dust basic properties of our sample sources (Group II)

HIP (1)	Distance(pc) (2)	$T_{\text{eff}}$ (3)	$\log g$ (4)	E(B-V) (5)	$T_{\text{d}}$ (K) (6)	$R_{\text{d}}$ (AU) (7)	$M_{\text{d}}(M_{\oplus})$ (8)	$f_{\text{d}}$ (9)	Sp.Type (10)	References (11)
4683 <sup>†</sup>	446.4	10000	4.0	0.200	53	363	2.22e+02	1.53e-02	B5	1
4789	357.1	11000	4.0	0.093	106	145	3.59e+00	1.55e-03	B9	1,4
7345	61.3	9500	4.5	0.028	77	60	3.05e-01	7.65e-04	A1V	1,2,4,10
8851	411.5	10500	4.0	0.200	136	31	5.47e-02	4.89e-04	B8	...
11847	63.7	8000	4.5	0.178	90	22	7.46e-02	1.36e-03	F0	2,5,10,11
13487 <sup>†</sup>	261.1	10000	4.0	0.200	41	367	1.55e+02	1.05e-02	B8	1
14043	243.9	20000	4.0	0.138	81	701	2.54e+00	4.71e-05	B7V	...
16188	353.4	8750	4.0	0.192	69	250	5.80e+00	8.43e-04	A0	...
17812	393.7	10000	4.0	0.157	79	128	2.92e+00	1.61e-03	B9	...
17941	331.1	9500	4.5	0.064	86	63	5.06e+00	1.14e-02	A0	...
20556	194.9	9750	4.0	0.200	75	154	1.43e+00	5.48e-04	A2	...
20884	118.1	13000	4.0	0.000	119	67	1.46e-01	2.96e-04	B3V	1
21898	537.6	8250	4.5	0.000	70	169	1.63e+01	5.17e-03	A0	...
23451	112.1	8500	4.0	0.200	96	23	2.75e-01	4.56e-03	A0	2,10
24052 <sup>†</sup>	159.2	10000	4.0	0.200	45	214	1.76e+01	3.48e-03	B9	...
26062	100.0	10000	4.0	0.048	134	18	1.33e-01	3.40e-03	B8	...
27296	325.7	15000	4.0	0.134	85	247	5.18e+00	7.69e-04	B8	...
27321	19.3	8500	4.5	0.010	120	16	8.08e-02	2.85e-03	A3V	1,2,6,7,10,12,13
32345	454.5	10500	4.0	0.002	67	272	8.01e+00	9.86e-04	B9	...
36437	490.2	14000	4.0	0.034	98	219	4.13e+00	7.84e-04	B3IV/V	...
36581	666.7	8750	4.5	0.011	93	142	7.12e+00	3.22e-03	F8	...
40016 <sup>†</sup>	500.0	16000	4.0	0.008	37	2500	3.48e+02	5.07e-04	B3IV	1
40024	450.5	11500	4.0	0.003	82	158	1.43e+01	5.18e-03	B6V	...
40748	763.4	10000	4.0	0.036	86	71	7.56e+00	1.35e-02	B4	...
41650	288.2	9250	4.0	0.101	194	12	8.48e-01	4.73e-02	A0IV	1
46021	458.7	9750	4.0	0.098	77	112	5.23e+00	3.78e-03	A0III/IV	...
48613	97.8	10000	4.0	0.000	83	80	1.79e-01	2.50e-04	A0V	4
53524	91.6	9250	4.5	0.169	70	58	2.79e-01	7.41e-04	A8III	2,4
55505	46.7	4750	4.0	0.184	139	4	1.67e-01	6.16e-02	K4V	2
61498	67.1	10000	4.5	0.001	101	36	5.26e-01	3.68e-03	A0V	2,3,10,13
65875	97.1	7250	4.5	0.154	95	21	1.52e-01	2.90e-03	F6V	...
73145	111.1	9250	4.5	0.096	97	25	1.86e-01	2.53e-03	A2IV	2,10
74421	260.4	10250	4.0	0.053	27	1851	2.25e+02	5.97e-04	B8/B9III	...
76736	77.3	9500	4.5	0.030	75	55	1.68e-01	4.95e-04	A5V	2

Table 3—Continued

HIP (1)	Distance(pc) (2)	$T_{\text{eff}}$ (3)	$\log g$ (4)	E(B-V) (5)	$T_{\text{d}}$ (K) (6)	$R_{\text{d}}$ (AU) (7)	$M_{\text{d}}(M_{\oplus})$ (8)	$f_{\text{d}}$ (9)	Sp.Type (10)	References (11)
77441	117.0	7500	4.5	0.109	63	55	4.03e-01	1.18e-03	F2/F3V	...
79977	131.8	7250	4.5	0.190	87	23	4.17e-01	6.77e-03	F2/F3V	4
81474	165.0	10000	4.0	0.200	78	144	2.32e+00	1.01e-03	B9.5IV	1
81891	240.4	12000	4.0	0.001	87	155	1.43e+00	5.37e-04	B8V	...
83505	342.5	10000	4.0	0.200	71	175	5.86e+00	1.74e-03	B9.5III	...
86078	317.5	8250	4.0	0.197	62	215	4.43e+00	8.70e-04	A0	...
87807	207.9	11750	4.0	0.200	74	129	1.11e+00	6.04e-04	B9	...
88399	46.9	7750	4.5	0.194	76	29	5.16e-02	5.54e-04	F5V	2,5,10,12
90491	117.5	8250	4.5	0.008	67	35	4.41e-01	3.13e-03	A0	...
91262	7.8	10000	4.0	0.022	65	146	2.45e-02	1.04e-05	A0V	1,2,6,7,13
92800	225.7	10000	4.0	0.095	72	174	7.04e+00	2.10e-03	A0	1
93000	354.6	10000	4.0	0.200	75	243	1.09e+01	1.68e-03	B8II/III	...
95270	50.6	6500	4.0	0.001	78	22	1.68e-01	3.05e-03	F5/F6V	2,10,12
95619	69.1	10250	4.0	0.009	76	72	1.66e-01	2.90e-04	B8/B9V	2,10
99273	53.5	6500	4.0	0.001	91	16	5.22e-02	1.82e-03	F5V	2,9,10
102761	431.0	18000	4.0	0.194	81	334	1.45e+01	1.18e-03	B8	...
104354	555.6	14000	4.0	0.184	98	185	3.68e+00	9.74e-04	B9	...
111214	393.7	11500	4.0	0.200	69	160	3.07e+00	1.09e-03	B9	...
111429	289.9	14000	4.0	0.015	53	462	9.71e+00	4.14e-04	B1.5V	...
113368	7.7	8750	4.0	0.008	54	107	6.30e-02	4.98e-05	A3V	1,2,5,6,7,8,13
118289	300.3	18000	4.0	0.142	103	195	2.24e+00	5.32e-04	B9	1

Note. — <sup>†</sup> SED fitting with 2 blackbody model.

Note. — Col.(1): *Hipparcos* identification. Col.(2): Distance. Col.(3): Effective temperature. Col.(4): Surface gravity. Col.(5): E(B-V). Col.(6): Dust temperature. Col.(7): Dust location. Col.(8): Total dust mass( $M_{\oplus}$ ). Col.(9): Dust fractional luminosity. Col.(10): Spectral type. Col.(11): References – (1)Oudmijer et al. 1992; (2)Rhee et al. 2007; (3)Koerner et al. 1998; (4)Chen et al. 2006; (5)Decin et al. 2003; (6)Habing et al. 1999; (7)Habing et al. 2001; (8)Su et al. 2006; (9)Carpenter et al. 2008; (10)Moór et al. 2006; (11)Moór et al. 2011; (12)Rebull et al. 2008 (13)Rieke et al. 2005

## REFERENCES

- Abraham, P., Leinert, C., Burkert, A., Lemke, D., Henning, T. 1999, *A&A*, 338, 91
- Allam, S., Assendorp, R., Longo, G., Braun, M., & Richter, G. 1996, *A&AS*, 117, 39
- Armitage, P. J. 2007, *ArXiv Astrophysics e-prints*, arXiv:astro-ph/0701485
- Assendorp, R., Bontekoe, T. R., de Jonge, A. R. W., et al. 1995, *A&AS*, 110, 395
- Aumann, H. H., et al. 1984, *ApJ*, 278, L23
- Backman, D. E., & Paresce, F. 1993, in *Protostars and Planets III*, ed. V. Mannings, A.P. Boss, & S. S. Russell (Tucson: Univ. Arizona Press), 1253
- Beichman, C. A., Bryden, G., Stapelfeldt, K. R. et al. 2006, *ApJ*, 652, 1674
- Bessell, M. 2000, *PASP*, 112, 961
- Booth, M., Kennedy, G. et al. 2013, *MNRAS*, 428, 1263
- Boulanger, F., & Pérault, M. 1988, *ApJ*, 330, 964
- Bryden, G. et al. 2006, *ApJ*, 636, 1098
- Carpenter, J. M., Bouwman, J. et al. 2008, *ApJS*, 179, 423
- Castelli, F. & Kurucz, R. L. 2004, arXiv:astro-ph/0405087
- Chen, C. H., Patten, B. M., Werner, M. W., Dowell, C. D., Stapelfeldt, K. R., Song, I., Stauffer, J. R., Blaylock, M., Gordon, K. D., Krause, V. 2005, *ApJ*, 634, 1372
- Chen, C.H., et al. 2006, *ApJS*, 166, 351
- Cox, A. N., ed. 2000, *Allen’s Astrophysical Quantities*
- Decin, G., Dominik, C., Waters, L. B. F. M., Waelkens, C. 2003, *ApJ*, 598, 636
- Eiroa, C., Marshall, J. P. et al. 2011, *A&A*, 536, 4
- Eiroa, C., Marshall, J. P. et al. 2013, *A&A*, 555, 11
- Fajardo-Acosta, S. B., Stencel, R. E., Backman, D. E., Thakur, N. 1999, *ApJ*, 520, 215
- Fujiwara, H., Yamashita, T., et al. 2009, *ApJ*, 695, 88
- Fujiwara, H., Onaka, K., et al. 2010, *ApJ*, 714, 152

- Fujiwara, H., Ishihara, D., et al. 2010, *cosp*, 38, 2470
- Fujiwara, H., Ishihara, D., et al. 2013, *A&A*, 550, 45
- Greaves, J. S., Holland, W. S., Wyatt, M. C., et al. 2005, *ApJ*, 619, 187
- Habing, H., Dominik, C., Jourdain de Muizon, M., et al. 1999, *Nature*, 401, 456
- Habing, H., Dominik, C., et al. 2001, *A&A*, 365, 545
- Kalas, P., Graham, J. R., Beckwith, S. V. W., Jewitt, D. C., Lloyd, J.P. 2002, *ApJ*, 567, 999
- Kalas, P., Graham, J. R., Clampin, M. C., Fitzgerald, M. P. 2006, *ApJ*, 637, 57
- Kawada, M., Baba, H., et al. 2007, *pasj*, 59, 389
- Kessler, M. F., Steinz, J. A., et al. 1996, *A&A*, 315, 27
- Kim, J. S., Hings, D. C., Rivinius 2005, *ApJ*, 632, 659
- Koerner, D. W., Ressler, M. E., Werner, M. W., Backman, D. E. 1998, *ApJ*, 503, 83
- Krivov, A.V. 2010, *raa*, 10, 383
- Lagrange, A.M., Milli, J., Boccaletti, A. et al. 2012, *A&A*, 546, 38
- Maldonado, J., Eiroa, C. et al. 2012, *A&A*, 541, 40
- Matthews, B. C., Sibthorpe, B., Kennedy, G. et al. 2010, *A&A*, 518, 135
- Mannings, V., Barlow, M. J. 1998, *ApJ*, 497, 330
- Meyer, M.R., et al. 2008, *ApJ*, 673, L181
- Moór, I., Abraham, P., Derekas, A. et al. 2006, *ApJ*, 644, 525
- Moór, I., Pascucci, A. et al. 2011, *ApJS*, 193, 4
- Neugebauer, G., Habing, H. J., et al. 1984, *ApJ*, 278, 1
- Olofsson, J., Juhaász, A. et al. 2012, *A&A*, 542, 90
- Oudmaijer, R. D., van der Veen, W. E. C. J. et al. 1992, *A&A*, 96, 625
- Perryman, M.A.C., Lindegren, L., et al. 1997, *A&A*, 323, L49
- Plavchan, P., Werner, M. W., Chen, C. H. et al. 2009, *ApJ*, 698,1068

- Porter, J., Rivinius, T. 2003, PASP, 115, 1153
- Raymond, S. N., Armitage, P. J. et al. 2011, A&A, 530, 62
- Raymond, S. N., Armitage, P. J. et al. 2012, A&A, 541, 11
- Rebull, L.M., et al. 2008, ApJ, 681, 1484
- Rhee, J. H., Song, I. R., Zuckerman, B., McElwain, M. 2007, ApJ, 660, 1556
- Ribas, A., Meriñ, B. et al. 2012, A&A, 541, 38
- Rieke, G. H., Young, E. T., Engelbracht, C. W., et al. 2004, ApJS, 154, 25
- Rieke, G.H., et al. 2005, ApJ, 620, 1010
- Schneider, G. et al. 2001, ASPC, 244, 203S
- Schutz, O., Meeus, G., Sterzik, M. F. 2005, A&A, 431, 175
- Siegler, N., Muzerolle, J., Young, E. T., Rieke, G. H., Mamajek, E. E., Trilling, D. E., Gorlova, N., & Su, K. Y. L. 2007, ApJ, 654, 580
- Silverstone M. 2000, *The Vega phenomenon: evolution and multiplicity*. PhD thesis. Univ. Calif., Los Angeles. 194 pp.
- Skrutskie, M. F., Cutri, R. M., Weinberg, M. D. et al. 2006, AJ, 131, 1163
- Spangler, C., et al. 2001, ApJ, 555, 932S
- Su, K. Y. L., Rieke, G. H., Stansberry, J. A., Bryden, G. et al. 2006, ApJ, 653, 675
- Su, K. Y. L., Rieke, G. H., Stapelfeldt, K. R. et al. 2008, ApJ, 679, 125
- Urban, L. E., Rieke, G. et al. 2012, ApJ, 750, 98
- Werner, M. W., Roellig, T. L., Low, F. J., et al. 2004, ApJS, 154, 1
- Wright, E. L., et al. 2010, AJ, 140, 1868
- Wu, H., Wu, C. J., Cao, C. 2012, raa, 12, 513
- Wyatt, M. C. , Greaves, J. S., Dent, W. R. F., Coulson, I. M. 2005, ApJ, 620, 492
- Wyatt, M. C. 2008, ARA&A, 46, 339
- Yamamura, S., et al. 2010, cosp, 38, 2496Y



Zuckerman, B., & Song, I. 2004, ApJ, 603, 738